

# Flow Patterns in the Vicinity of Triple Line Dynamics Arising from a Local Surface Tension Model

*J. Monnier, A. M. Benselama, and I. Cotoi*

LJK - MOISE Project-Team, BP 53, F-38041 Grenoble  9, France

## ABSTRACT

---

*We model and simulate numerically a droplet impact onto a solid substrate. The triple line dynamics modeling is implicit (as opposed to classical explicit mobility relations); it is based on the Shikhmurzaev equations. These equations include generalized Navier slip type boundary conditions with extra local surface tension gradient terms. Numerical results when spreading are presented. A particular attention is paid to flow patterns near the contact line.*

---

\*Address all correspondence to 

## 1. INTRODUCTION

One of the main difficulties in simulating present droplet flows is the contact line dynamics modeling. This problem has been widely studied and still remains an open problem. Let us cite macroscopic models with slip boundary conditions (see, e.g., [1–3]), mesoscopic models with diffuse interface (see, e.g., [4,5], and connection with molecular dynamics (see, e.g., [6]). The most frequent contact line model is an explicit mobility relation giving the contact line velocity in function of the wetting angle value at any time (Tanner type laws). Nevertheless, it has been shown, [7] that the dynamic wetting angle cannot be determined inherently by such a mobility relation.

In the present paper, we consider an “implicit” model based on the Shikhmurzaev theory [7,8]. This model led to generalized Navier slip type boundary conditions with local surface tension gradient terms. It does not impose the contact line velocity nor the wetting angle since they are a response of the full model. In Section 2, we present the equations: 2D axisymmetric Navier-Stokes equations with an ALE formulation. In Section 3, we discretize the equations using a finite element scheme. We introduce a contact line algorithm that imitates the caterpillar motion observed in experiments. Curvature is computed using a local Bezier least-squares approximation. In Section 4, first we consider a Tanner-type law and we test the robustness of our algorithm. Then, we consider both spreading phase and recoiling phase, using the present “implicit” model based on the Shikhmurzaev theory. The extra local terms appearing in this model are set by preliminary results presented in [9,10]. We show different flow patterns generated by these terms near the triple point. Finally, we obtain encouraging results for both phases.

## 2. MATHEMATICAL MODEL

### 2.1 The Equations

The droplet dynamics is modeled by the 2D axisymmetric unsteady incompressible Navier-Stokes equations. We denote by  $\vec{u} = (u_r, u_z)^T$  the fluid velocity,  $p$  its pressure,  $\Sigma$  the stress tensor,  $D$  the deformation, tensor and  $\text{Re}$  the Reynolds number. We denote by  $(\vec{\tau}, \vec{n})$  the unit tangential and exter-

nal normal vectors such that it is direct. We set  $\vec{\Sigma}_n = \Sigma \cdot \vec{n}$ ,  $\vec{\Sigma}_n = \Sigma_n \vec{n} + \Sigma_\tau \vec{\tau}$ .

#### 2.1.1 Free Surface Dynamics and ALE Formulation

The free surface  $\Gamma_{fr}$  is transported by the velocity field  $\vec{u}$ . It is described by an implicit function,  $\phi(t, x(t), y(t), z(t)) = 0$ , and we have

$$\frac{d\phi}{dt} = \frac{\partial\phi}{\partial t} + \vec{u} \cdot \nabla\phi = 0 \quad \text{in } (0, T) \times \Omega \quad (1)$$

with given initial conditions. We present the ALE formulation, we use as well as the characteristics method. We refer to [11,12]. The principle of the ALE method is to define an equivalent velocity field  $\vec{\gamma}$  (in the sense  $\vec{\gamma} \cdot \vec{n} = \vec{u} \cdot \vec{n}$  on  $\partial\Omega$ ) such that it preserves the mesh inside the fluid domain  $\Omega$ . To this end, at any time  $t$ , we define the deformation field  $\vec{\gamma}$  on the free surface  $\Gamma_{fr}$ , then we extend it all over the domain by solving a linear elasticity system.

Let  $t \mapsto C(x, \tau; t)$  be the characteristics lines associated to the velocity field  $\vec{\gamma}$ , then one can define the ALE variables:  $\vec{u}^\tau = \vec{u} \circ C$  and  $p^\tau = p \circ C$ . In the ALE space, fluid particles have a velocity  $(\vec{u} - \vec{\gamma})$  at first order in time  $(t - \tau)$ . And for  $t = \tau$ , one has  $\partial\vec{u}/\partial t = \partial\vec{u}^\tau/\partial t - \vec{\gamma}^\tau \cdot \nabla\vec{u}^\tau$ , with  $\vec{\gamma}^\tau = \vec{\gamma} \circ C$ .

If we denote by  $t \mapsto X(x, \tau; t)$  the Lagrangian characteristic lines (i.e., those associated to the velocity field  $\vec{u}$ ), the ALE method consists of defining a regular field  $\vec{\gamma}$  such that  $\Gamma_{fr}^t = C(\Gamma_{fr}^0, t^0; t) = X(\Gamma_{fr}^0, t^0; t)$ .

The  $r$ -momentum equation with ALE formulation is

$$\begin{aligned} \text{Re} \left( \frac{\partial u_r^\tau}{\partial t} + (\vec{u}^\tau - \vec{\gamma}) \cdot \nabla u_r^\tau \right) &= -\frac{\partial p^\tau}{\partial r} \\ + 2 \left( \frac{1}{r} \frac{\partial [r D_{rr}(\vec{u}^\tau)]}{\partial r} + \frac{\partial [D_{rz}(\vec{u}^\tau)]}{\partial z} - \frac{u_r^\tau}{r^2} \right) & \quad (2) \end{aligned}$$

The  $z$ -momentum equation is similar. The continuity equation is

$$\frac{1}{r} \frac{\partial (r u_r^\tau)}{\partial r} + \frac{\partial u_z^\tau}{\partial z} = 0$$

with initial conditions. Boundary conditions on the free surface (liquid-gas) are

$$\vec{\Sigma}_n = \left( -p_{\text{ext}} + \frac{\kappa^\tau}{\text{Ca}} \right) \vec{n} + h \vec{\tau} \quad \text{in } (0, T) \times \Gamma_f \quad (3)$$

where  $Ca$  is the capillary number,  $\kappa$  is the mean curvature, and  $p_{\text{ext}}$  is the external pressure. The extra term  $h$  is given (see Shikhmurzaev's theory [8], Section 2.2.2). We have classical boundary conditions on the symmetry axis. We decompose the liquid-solid interface into two parts,  $\Gamma_{ad}$  and  $\Gamma_{sl}$ .  $\Gamma_{sl}$  denotes a "small" part of the liquid-solid interface near the triple point. We consider a generalized Navier slip-type boundary condition (local slipping),

$$\begin{cases} \vec{u}^\tau \cdot \vec{n} = 0 & \text{in } (0, T) \times \Gamma_{sl} \\ \Sigma_\tau = -[\beta \vec{u}^\tau + \vec{g}] \cdot \vec{\tau} & \text{in } (0, T) \times \Gamma_{sl} \end{cases} \quad (4)$$

where  $\beta$  is a given sliding coefficient. The extra term  $\vec{g}$  is given; it models either a surface tension gradient in the Shikhmurzaev's theory or a uncompensated Young stress in the Qian-Wang-Sheng theory [13], see Section 2.2.4. On  $\Gamma_{ad}$ , we impose adherence boundary conditions:  $\vec{u} = 0$ .

The solution  $(\vec{u}^\tau, p^\tau) \circ C$  is an approximation of  $(\vec{u}, p)$  at first order in time, and curvatures  $\kappa^\tau$  approximates  $\kappa$  at first order in time, too (see, e.g., [12]). In all the sequels we simplify notations by dropping the arrows  $\vec{\cdot}$  and the superscript  $\tau$ .

## 2.2 Contact Line Dynamics Modeling

We consider two different types of model for the contact line dynamics, an explicit model (Tanner-type law) and an "implicit" one deriving from Shikhmurzaev theory.

### 2.2.1 Mobility Relation (Tanner-Type Law)

The contact line velocity and the wetting angle are related by

$$U_{\text{CL}}(t) = k \frac{[\theta(t) - \theta^{eq}]^\gamma}{(\theta^{eq})^\gamma} \quad \text{for } t \in ]0, T[ \quad (5)$$

where  $U_{\text{CL}}$  is the contact line velocity, and  $\theta^{eq}$  is the wetting angle at equilibrium (Young's law),  $\theta$  is the (dynamic) wetting angle.  $k$  and  $\gamma$  are parameters usually determined using experimental results.

### 2.2.2 Local Flow modeling and Shikhmurzaev's Theory

The "implicit" model does not impose the contact line velocity and the wetting angle but considers them as a response of the model. This model is

based on Shikhmurzaev's theory [7,8], which introduces the generalized Navier slip condition (4) and the condition (3). These conditions are local since the extra terms  $\vec{g}$  and  $h$  vanish except in the vicinity of the triple point. The basic idea of this theory is to consider that the rolling motion observed in experiments [5] implies that particles of the liquid-gas interface, which become an element of the solid-liquid, lose their properties in a finite time. Then, the surface tension value associated to this particle must change to its new equilibrium value relative to the solid-liquid interface. This process would give rise to a surface tension gradient in a small vicinity of the advancing contact line (hence, a local Marangoni effect). In other respects, the Young equation would remain valid at any time. In this theory,

$$\vec{g} = -\frac{1}{2Ca} \vec{\nabla} \sigma \quad \text{and} \quad h = \frac{1}{Ca} \vec{\nabla} \sigma_{\text{LG}} \cdot \vec{\tau} \quad (6)$$

where  $\sigma$  and  $\sigma_{\text{LG}}$  are the liquid-solid and the liquid-gas surface tension coefficients, respectively. In [9,10], a mathematical and numerical study presents some qualitative behaviors of  $g$  and  $h$  arising from Shikhmurzaev's theory see Fig. 1.

### 2.2.3 The Mesoscopic Local Surface Model (LSM)

Briefly, the so-called mesoscopic LSM, as it is established in [8], is as follows. The interfaces are described by surface densities  $\rho^s$  (a variable that describes unambiguously the surface state). These surface densities are solutions of the surface continuity equations. A linear state equation gives the relation between  $\rho^s$  and the surface tension coefficients  $\sigma$ . We denote by  $\rho_i^s$ ,  $i = 1, 2$ , the surface density on  $\Gamma_{fr}$  ( $i = 1$ ) and on  $\Gamma_{\text{solid}}$  ( $i = 2$ ), by  $\sigma_1 = \sigma$  and  $\sigma_2 = \sigma_{\text{SL}}$ . The surface tension is related to the excess density through the linear state equation,

$$\sigma_i = \gamma(\rho_0^s - \rho_i^s) \quad i = 1, 2 \quad (7)$$

where  $\gamma$  and  $\rho_0^s$  are given constants. According to [14],  $\gamma \approx 2 \cdot 10^6$  and  $\rho_0^s \approx 10^{-7}$ .

We have the surface continuity equation

$$\frac{\partial \rho_i^s}{\partial t} + \text{div}(\rho_i^s \vec{v}_i^s) + \frac{1}{\tau^*} (\rho_i^s - \rho_i^{eq}) = 0 \quad i = 1, 2 \quad (8)$$

where  $\tau^*$  is the relaxation time relative to the rolling motion,  $\tau^* \approx 10^{-3}$  (see [3]),  $\vec{v}_i^s$  is a mean velocity inside the layer and  $\rho_i^{eq}$  is its density at equilibrium [16]:  $\sigma_i(\rho_i^{eq}) = \sigma_i^{eq}$ ,  $i = 1, 2$ .

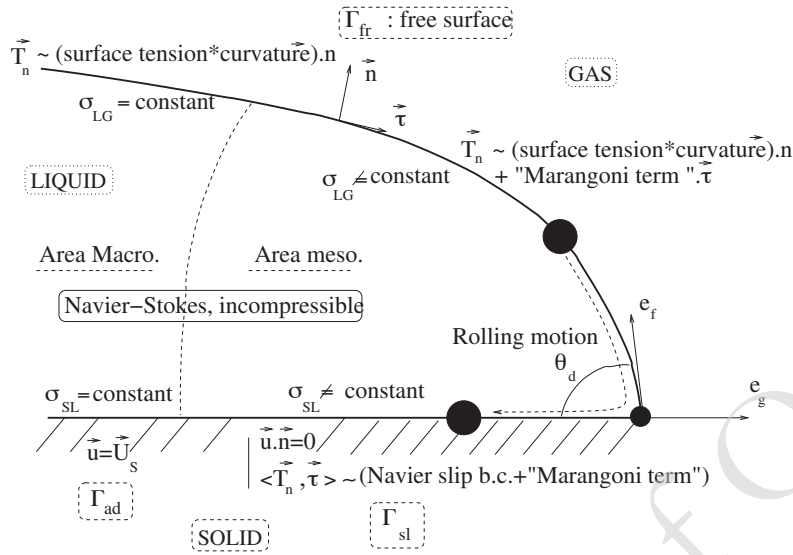


Figure 1. Advancing angle and Shikhmurzaev's model

The velocity  $\vec{v}_1^s$  (respectively,  $\vec{v}_2^s$ ) is related to  $\rho_1^s$  (respectively  $\rho_2^s$ ) and to the fluid velocity  $\vec{u}$ . We have the following Darcy laws type [8]:

$$(1 + 4\alpha_1\alpha_2)\vec{\nabla}\sigma_{fr} = 4\alpha_2(\vec{v}_1^s - \vec{u}) \quad \text{and} \quad \vec{v}_2^s = \alpha_1\vec{\nabla}\sigma_{solid} + \frac{1}{2}\vec{u} \quad (9)$$

where  $\alpha_i$ ,  $i = 1, 2$ , are given constants characterizing the viscous properties of the interface. According to [14],  $\alpha_1 \approx h/\mu$ ,  $h$  being the surface layer thickness,  $h \approx 10^{-10}$ .

At the triple line, the surface flux continuity is imposed as

$$(\rho_1^s \vec{v}_1^s) \vec{e}_f = (\rho_2^s \vec{v}_2^s) \vec{e}_g \quad (10)$$

where  $\vec{e}_f$  and  $\vec{e}_g$  are unit vectors normal to the contact line and tangential to the gas-liquid and gas-solid interfaces, respectively. Let us note that  $\cos(\theta) = -\vec{e}_f \cdot \vec{e}_g$ .

*Remark.* The most important feature of the Shikhmurzaev model is supposed to be the following. It does not impose either the contact line velocity nor the wetting angle since both are a full response of the model. Nevertheless, the LSM is constituted by the two surface equations (8) and the boundary condition (10) at the contact line. Then, as it is noted in [14], the condition (10) at the contact line is not enough to close the system. To this end,

the problem misses an extra condition at the contact line. This can be very easily shown for some linear second-order differential equations with only a flux continuity condition at the junction point. The missing condition cannot be the Young equation because otherwise it would imply that the wetting angle must be given, and it would not be a response of the model anymore. The author of [14] proposes an extra condition of the following type:

$$(\rho_1^s \vec{v}_1^s) \vec{e}_f = F(\rho_1^s, \rho_2^s) \quad (11)$$

where  $F(\rho_1^s, \rho_2^s)$  is a bilinear given function related to a chemical potential law.

## 2.2.4 A Connection with Qian-Wang-Sheng Theory

From molecular dynamics simulations on immiscible fluids, the authors of [6,13] and show that the relative slipping between the fluid and the solid wall follows a generalized Navier slip boundary condition similar to (4). In this theory, the extra term  $\vec{g}$  in (4) would model the contribution of the tangential stress due to nonshear stress that appears because of the anisotropy of the pressure (thus its nonshear origin) across the fluid-fluid interface; the normal pressure term is no longer equal to the tangential pressure term across this interface, since this usually occurs in the bulk. Hence this term, which is present as

far as the two(fluid)-phase region is involved, is connected to the fluid-fluid interfacial tension. The extra tangential stress  $\vec{g}$ , called interfacial uncompensated (or unbalanced) Young stress, is defined as follows:  $\int_{\Gamma_{\text{int}}} g dy = \sigma(\cos \theta - \cos \theta^{eq})$ , where  $\int_{\Gamma_{\text{int}}} dy$  denotes the integral across the interface  $\Gamma_{fr}$ .

From a macroscopic point of view, it is obvious that it arises from the deviation of the fluid-fluid interface from its static configuration and is narrowly distributed in the fluid-fluid interface region. Therefore, both theories (Shikhmurzaev's and the molecular one) lead to such a generalized Navier slip boundary condition [Eq. (4)]. The derivation and the interpretation of the extra term  $\vec{g}$  is different for each theory, but from a mathematical modeling point of view, the boundary condition is similar. Moreover, the authors of [6,13] point out the fact that, independently of the nearness to the fluid-fluid interface, the generalized Navier slip condition is a more general and suitable condition than the classical nonslip condition, provided slip coefficient  $\beta$  and  $\vec{g}$  are well adjusted.

### 3. DISCRETIZATION AND ALGORITHMS

#### 3.1 Finite Element Scheme

We discretize the full model in time using the Euler implicit scheme and a first-order characteristic method. Let  $\{t_0 = 0, t_1, \dots, t_M = T\}$  be a discretization of  $]0, T[$  with a constant time step  $\Delta t = \frac{T}{M}$ . The semidiscrete  $r$ -momentum equation is (similar discretization of  $z$ -momentum equation is done)

$$\text{Re} \frac{u_r^{m+1} - u_r^m \circ \chi^m}{\Delta t} = -\frac{\partial p^{m+1}}{\partial r} + 2 \times \left( \frac{1}{r} \frac{\partial [r D_{rr}(\vec{u}^{m+1})]}{\partial r} + \frac{\partial [D_{rz}(\vec{u}^{m+1})]}{\partial z} - \frac{u_r^{m+1}}{r^2} \right) \quad (12)$$

and

$$\text{Re} \frac{u_z^{m+1} - u_z^m \circ \chi^m}{\Delta t} = -\frac{\partial p^{m+1}}{\partial z} + 2 \left( \frac{1}{r} \frac{\partial [r D_{zr}(\vec{u}^{m+1})]}{\partial r} + \frac{\partial [D_{zz}(\vec{u}^{m+1})]}{\partial z} \right) \quad (13)$$

where the superscript  $m$  represents the evaluation of the quantity at  $t = t_m$  and  $\chi^m$  denotes the characteristic associated to the velocity field  $(\vec{u} - \vec{\gamma})$ , defined by

$$\begin{cases} \frac{d\chi^m}{dt}(t) = (\vec{u} - \vec{\gamma})(\chi^m(t), t) & t \in ]t^m, t^{m+1}[ \\ \chi^m(t^{m+1}) = \mathbf{x} \end{cases} \quad (14)$$

Then,  $\chi^m(x)$  is approximated by  $\chi^m(x) \approx x - \Delta t(\vec{u}^m - \vec{\gamma}^m)(x)$ . The semidiscrete  $z$ -momentum equation is similar.

We set

$$\vec{u}_{ax} = \left( \frac{u_r}{r^2}, 0 \right)^T$$

and we denote  $\div_{rz}(\cdot) = \frac{1}{r} \frac{\partial}{\partial r}[r(\cdot)] + \frac{\partial}{\partial z}(\cdot)$ . Then, we can write (12) and (13) as follows:

$$\begin{aligned} \lambda \vec{u}^{m+1} - 2 \div_{rz}[D(\vec{u}^{m+1})] + \nabla p^{m+1} \\ + 2\vec{u}_{ax}^{m+1} = \lambda(\vec{u}^m \circ \chi^m) \end{aligned} \quad (15)$$

with  $\lambda = \frac{\text{Re}}{\Delta t}$ .

Let us recall that  $(\vec{u}, p)$  does not denote the Eulerian velocity pressure but its ALE counterpart. Equation (1) is semidiscretized using the Euler implicit scheme and the first-order characteristic method. This gives

$$\phi^{m+1} = \phi^m \circ X^m \quad \text{in } \Omega, \quad m = 1, 2, \dots \quad (16)$$

where  $X^m$  denotes the characteristic associated to the velocity field  $u$  at time  $t_m$ . It is approximated as follows:  $X^m(x) \approx x - \Delta t \vec{u}^m(x)$ .

The space discretization is done using the second-order Taylor-Hood finite element. The scheme is implemented using a public C++ finite element library Rheolef [15].

#### 3.2 ALE Free Surface Algorithm

The free surface problem is solved using an ALE formulation and a characteristics method. The algorithm (Fig. 2) is the following. At time step  $n$ , given  $\Omega^n$  and  $(\vec{u}^n, p^n)$  in  $\Omega^n$ .

*Step 1.* Compute the new free surface position  $\Gamma_f^n$  following the Lagrangian characteristic lines (each point of the boundary is translated by  $\vec{u}^n \Delta t$ ). Then, compute an equivalent deformation field  $\vec{\gamma}^n$  preserving the mesh by solving a linear elasticity system.

*Step 2.* Compute the new solution  $(\vec{u}_\tau^{n+1}, p_\tau^{n+1})$  of Navier-Stokes in  $\Omega^n$ .

*Step 3.* Update the domain  $\Omega^{n+1} = \vec{\gamma}^n(\Omega^n)$  (mesh transport by  $\vec{\gamma}^n$ ).

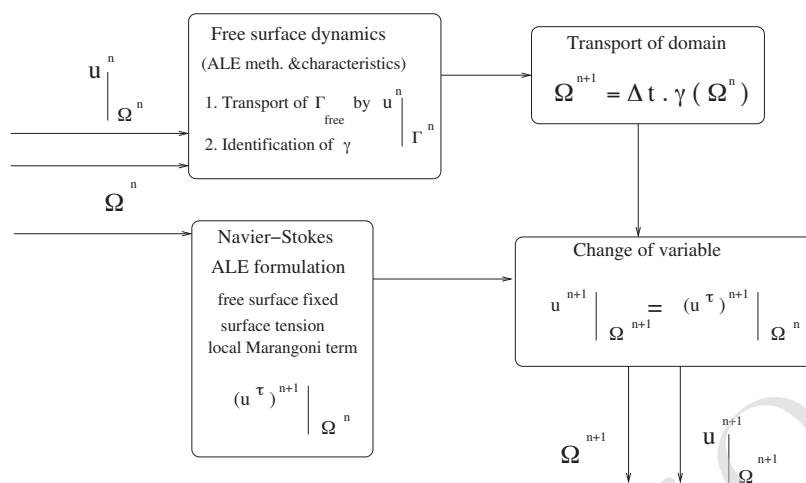


Figure 2. Algorithm of resolution

Step 3. Obtain the new solution  $(\bar{u}^{n+1}, p^{n+1})$  in  $\Omega^{n+1}$  by setting  $\bar{u}^{n+1}|_{\Omega^{n+1}} = \bar{u}_\tau^{n+1}|_{\Omega^n}$  and  $p^{n+1}|_{\Omega^{n+1}} = p_\tau^{n+1}|_{\Omega^n}$ .

surface is projected on the solid substrate, all the points on the solid wall but the last ones become no-slip points. The last two points remain slip points.

### 3.3 Spreading and Caterpillar Motion

When spreading, our algorithm imitates the caterpillar motion observed in experiments [1]. Figure 3 represents typical successive time steps. If at time step  $n$  the first point (or several points) on the free

### 3.4 Recoiling Motion

When dewetting (recoiling), the triple point and the slip points are allowed to move horizontally; also vertically if their vertical velocity is positive (see Fig. 4). If the triple point moves away from the

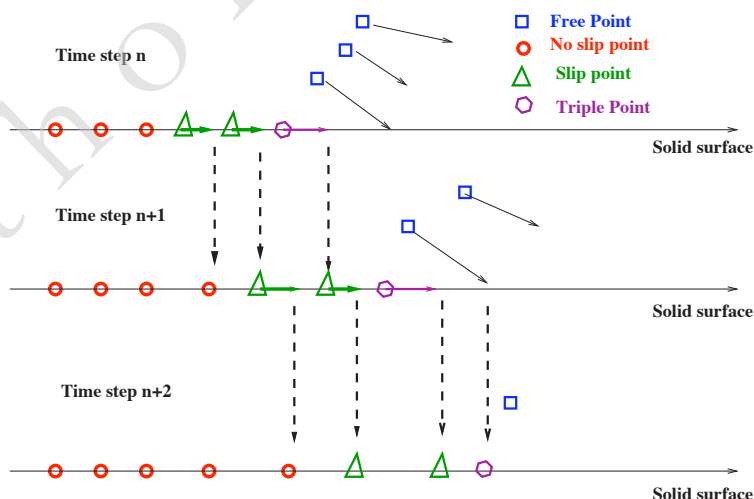
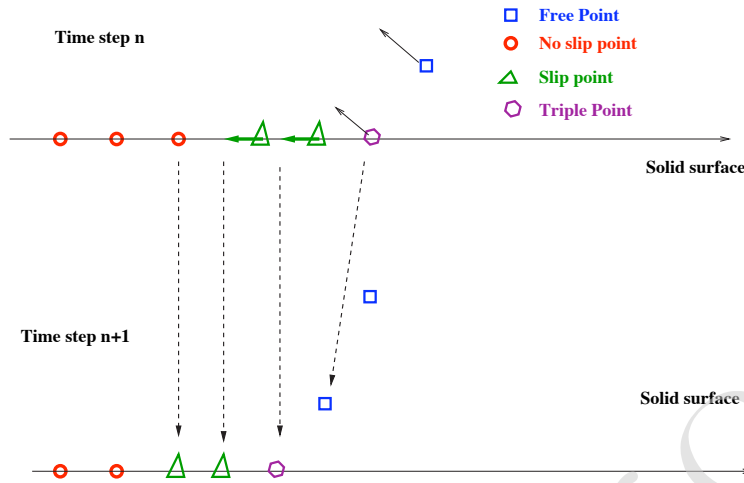


Figure 3. Spreading process. Circles represent no-slip nodes, triangles represent slip nodes  $u_z = 0$ , squares represent "free" nodes, diamond is the triple point



**Figure 4.** Recoiling process. Circles represent no-slip nodes  $\vec{u} = 0$ , triangles represent slip nodes  $u_z = 0$ , squares represent “free” nodes, diamond is the triple point

solid wall, the first point to the left becomes the triple point, hence becoming a free point. The second point to the left becomes a slip point.

**4. CURVATURE COMPUTATION**

We seek to compute the curvature of the droplet surface. Computing accurately the curvature is a difficult task since its interface is a piecewise linear curve, hence not  $C^2$  differentiable. In addition, points defining this piecewise linear curve result from the full free surface algorithm, hence may comprise some nonnegligible numerical errors. Then, we seek to estimate the curvature of an underlying smooth surface.

Computing a discrete surface curvature is a classical (and difficult) problem. Usually in the CAGD context, surfaces are 3D and triangularized, and the objectives are to smooth the mesh and to simplify it, but not to quantify a local variation of curvature (see, e.g., [16]).

The present problem is easier since the curve is 2D only, but we are facing the following dilemma: we seek to get rid of numerical errors connected to the points defining the curve while we seek to detect as accurate as possible local variations of curvature in order to obtain the resulting surface tension forces accurately. We do not consider a direct computation by a finite difference method since it is very sensitive to data error. We do not consider, neither, a polyno-

mial reconstruction of the underlying smooth surface then evaluate its curvature, since this leads to inaccurate results and unexpected behavior. Following [17], we consider a local least-squares approximation, then we evaluate the curvature. In the present algorithm, we consider a second-order local Bezier approximation. As the numerical tests show (see below), this method filters noise quite reasonably while it allows us to detect local and rapid variation of curvature.

**4.1 The Algorithm**

Given  $N$  points  $X_i = (r_i, z_i)^T, i = 1, \dots, N$ , defining the liquid-gas interface, the main idea is to approximate these data using a local least-squares approximation by a Bezier’s curve. The Bezier’s curve  $\mathcal{C}(t)$  is given by

$$\mathcal{C}(t) = [r(t), z(t)]^T = \sum_{j=1}^M P_j B_{j-1}^{M-1}(t) \quad \text{for } t \in [0, 1]$$

where  $P_j = (\alpha_j, \beta_j)^T \in \mathbb{R}^2$  are the control points and  $\{B_j^m(t)\}_{0 \leq j \leq M-1}$  is the classical Bernstein’s basis,  $B_j^m \in P_m, B_j^m(t) = C_j^m(1-t)^{m-j}t^j, C_j^m$  being the binomial coefficients.

We set  $M = 3$ , hence we consider three points of control  $P_j$  and second-degree curves. For an inner point  $X_i$ , see Fig. 5, we compute the least-square,

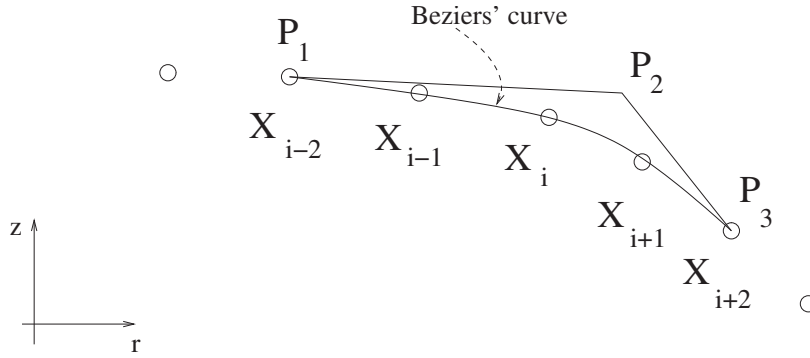


Figure 5. Inner point  $X_i$ . Local least square approximation using Bezier's curve

approximation of the five points  $\{X_{i-2}, \dots, X_{i+2}\}$  by a Bezier's curve as follows. We minimize

$$J(P_1, \dots, P_M) = \sum_{l=i-2}^{i+2} \left\| \sum_{j=1}^M P_j B_{j-1}^{M-1}(t_l) - X_l \right\|^2$$

where  $\{t_{i-2} = 0, \dots, t_{i+2} = 1\}$  is a uniform subdivision of  $[0, 1]$ . The unique minimum is computed by solving the corresponding normal equations.

For the extremal point  $X_1$ , we consider a Bezier's curve approximating the points  $X_i$  for  $i = 1, \dots, 4$ . For  $X_2$ , we consider a Bezier's curve approximating the points  $X_i$  for  $i = 1, \dots, 5$ . For the extremal points  $X_{N-1}$  and  $X_N$ , the principle is similar.

#### 4.1.1 Curvature Expression

Once a Bezier's curve  $\mathcal{C}(t) = [r(t), z(t)]^T$  is computed for each point  $X_i$ , we evaluate the (plane) curvature as follows:

$$\kappa_i = \kappa(t_i) = \frac{r'z'' - r''z'}{(r'^2 + z'^2)^{3/2}}(t_i)$$

where  $(r', z')$  and  $(r'', z'')$  are computed using de Casteljau's algorithm,  $t_i$  being the parameter value corresponding to  $X_i$ .

#### 4.1.2 Sensitivity to Random Noise

Since the control points defining the (optimal) droplet shape are resulting from the full free surface algorithm, they may be perturbed by some nonnegligible numerical errors. Hence, we test the robustness of our algorithm to data perturbation (see below).

If we denote  $N(r, z) = (r'z'' - r''z')$  and  $D(r, z) = (r'^2 + z'^2)^{3/2}$ , then:  $\kappa(r, z)(t) = [N(r, z)/D(r, z)](t)$ . Let  $\delta z$  be a perturbation on the  $z$  coordinate of data  $X_i$ ,  $i = 1, \dots, N$ , then we have

$$\frac{\partial \kappa}{\partial z}(r, z) \cdot \delta z = \frac{N(r, \delta z)}{D(r, z)} - 3 \frac{\kappa(r, z)}{(r'^2 + z'^2)} z' \delta z$$

This formula expresses the curvature sensitivity to perturbation on the  $z$  coordinate. Noise introduced in the numerical tests below is a random perturbation (on the  $z$  coordinate of data  $X_i$ ,  $i = 1, \dots, N$ ). It is a normal distribution with zero mean value and unit variance.

## 4.2 Numerical Tests

We present some numerical tests using the following two different methods:

*Method a.* Standard second-order finite difference scheme directly applied to the  $N$  data  $X_i = (r_i, z_i)^T$ ,  $i = 1, \dots, N$ .

*Method b.* Local approximation by a second-order Bezier's curve, then curvature computation.

In order to compare these two methods, we consider the following three curves (with noise introduced):

*Curve 1.* A circle, Fig. 6.

*Curve 2.* An "oscillating-curve," Fig. 7.

*Curve 3.* A "double circle," Fig. 8.

As mentioned above, noise is defined as a perturbation on the  $z$  coordinate of data  $X_i$ ,  $i =$

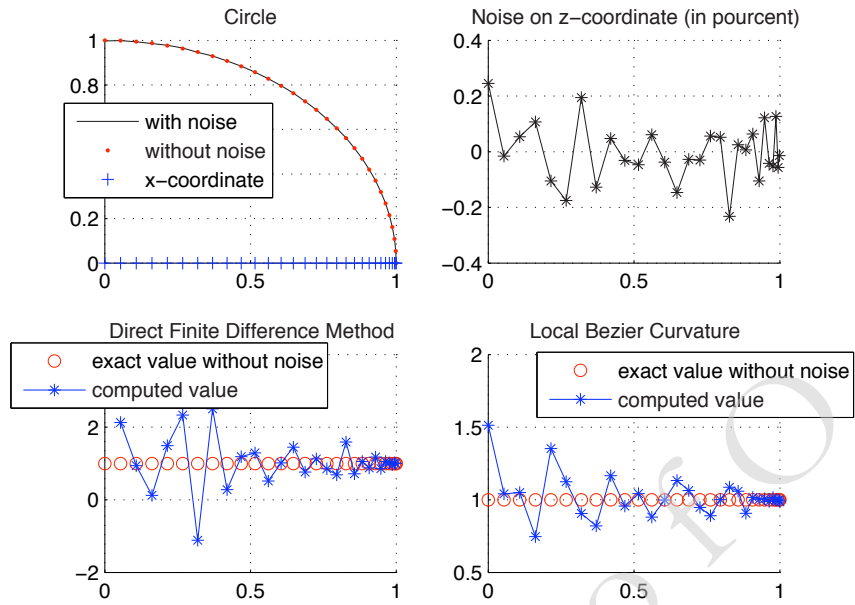


Figure 6. Curve 1 With noise introduced and computed curvature value

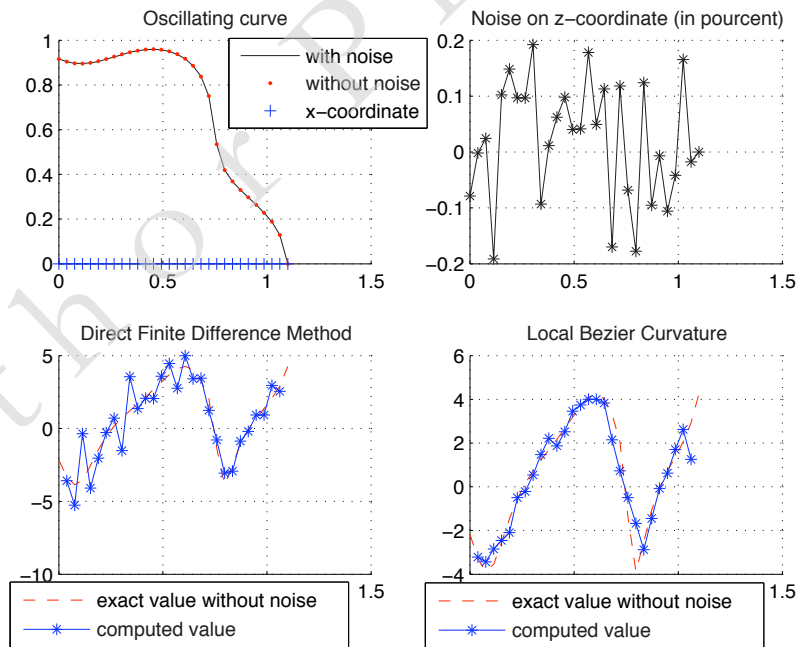


Figure 7. Curve 2 With noise introduced and computed curvature value

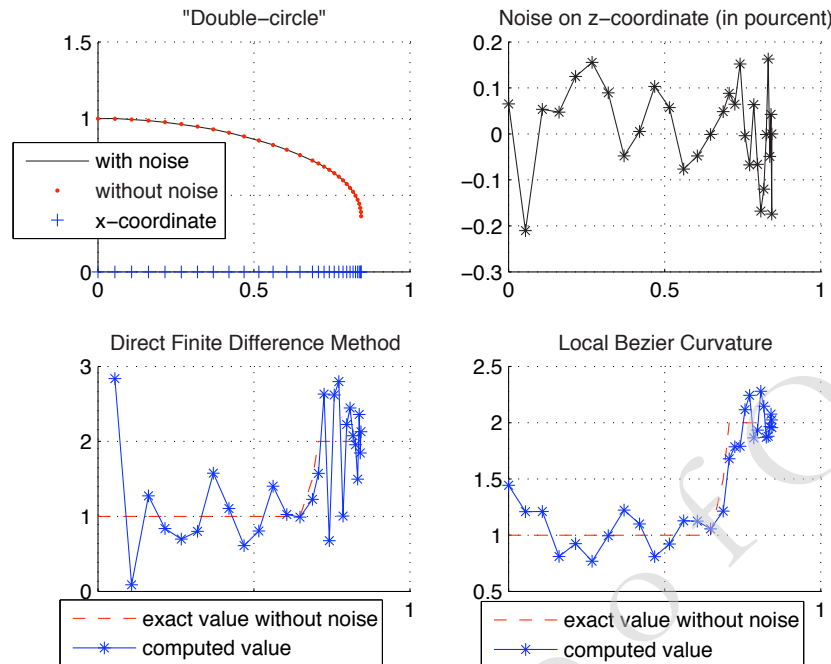


Figure 8. Curve 3 With noise introduced and computed curvature value

$1 \dots N$ . The circle is defined by  $N$  points as follows:  $r(i) = R \cos(\eta_i)$ ,  $z(i) = R \sin(\eta_i)$ , with  $\eta_i = [(i-1)\pi/2(N-1)]$ ,  $i = 1, \dots, N$ .

The so-called "oscillating-curve" is defined by  $N$  points as follows:  $r(s) = [R + \epsilon \cos(a \cdot s)] \cos(\pi/2s)$ ,  $z(s) = [R + \epsilon \cos(a \cdot s)] \sin(\pi/2s)$  with  $s \in [0, 1]$ ,  $s$  discretized by  $N$  points similarly to  $\eta$  and  $\epsilon = R/10$ ,  $a = 10$ . The exact curvature of the "oscillating-circle" is straightforwardly obtained. This curve is interesting since it presents smooth variations of curvature with change of sign.

The so-called double-circle is defined by  $N$  points as follows: For  $i = 1, \dots, M$ ,  $r(i) = R \cos(\eta_i)$ ,  $z(i) = R \sin(\eta_i)$ ; for  $i = M + 1, \dots, N$ ,  $r(i) = a + \frac{R}{2} \cos(\eta_i)$ ,  $a = (1 - R) \cos(\eta_M)$  and  $z(i) = b + \frac{R}{2} \sin(\eta_i)$ ,  $b = (1 - R) \sin(\eta_M)$ . This curve is interesting since it presents a sharp variation of curvature (noncontinuous, in fact).

We set  $R = 1$ ,  $M = 8$  and  $N = 30$ . Without noise (i.e., if considering the exact curves), the two methods allow us to retrieve perfectly the curvature values of the three curves.

In Figs. 6, 7, and 8, we also compare the two methods (a and b) by computing the curvature of

curves 1, 2, and 3 when some noise is introduced. In such a case, all our computational tests performed showed that method b gives much better results than method a. In other respects, we compared methods a and b with to a "global" method; we interpolated the given points using a parametric cubic spline, then we computed the curvature of the interpolating spline. This last method is much less accurate and much more sensitive to noise than methods a and b.

## 5. NUMERICAL RESULTS

We consider a water droplet. The reference length and velocity are  $L_{\text{ref}} = 2.3 \text{ mm}$ ,  $U_{\text{ref}} = 0.98 \text{ m/s}$ . Then,  $\text{Re} = \rho U_{\text{ref}} L_{\text{ref}} / \mu \approx 46$ , Weber number  $\text{We} = \rho U_{\text{ref}}^2 L_{\text{ref}} / \sigma \approx 68$ , and  $C_a = \sigma / \mu U_{\text{ref}} \approx 1.5$ .

### 5.1 Spreading Phase Using a Tanner-Type Law

We start by testing the efficiency of the algorithm. To this end, we consider the Tanner-type law as triple line dynamic modeling, and we make fit this law with available experimental data [18], related to a

spreading phase. The triple point position is imposed at each time. We focus on the volume conservation, the height and diameter of the spreading (splat radius), and the deformation of the mesh (number of remeshings necessary) (see Fig. 9). With a time step  $dt = 5 \times 10^{-5}s$  and a coarse mesh ( $\approx 600$  elements), the volume lost after 650 iterations is roughly 3%. The loss occurs mainly at the very beginning of spreading. Mesh transport is efficient, hence remeshing occurs only when a projection occurs (see previous section). From a qualitative point of view, numerical results are similar to experimental data [18].

### 5.2 Influence of the Local Parameters $(\beta, g, h)$

We present some influence of terms specific to the Shikhmurzaev’s model by considering the following steady-state Stokes system. Find  $(\vec{u}, p)$  such that

$$2 \int_{\Omega} D(\mathbf{u}) : D(\mathbf{v}) dx - \int_{\Omega} p \operatorname{div}(\mathbf{v}) dx \quad (17)$$

$$+ 2 \int_{\Omega} \mathbf{u}_a \mathbf{v} dx + \beta \int_{\Gamma_{slip}} u_r v_r ds$$

$$= \int_{\Gamma_{free}} \frac{\kappa}{Ca} \mathbf{v} \mathbf{n} ds + \int_{\Gamma_f} h \mathbf{v} \boldsymbol{\tau} ds - \int_{\Gamma_{sl}} g_r v_r ds, \quad \forall \mathbf{v}$$

$$\int_{\Omega} \operatorname{div}(\mathbf{u}) q dx = 0, \quad \forall q \quad (18)$$

We try to find the main effects of parameters  $\beta, \vec{g}, h$  from numerical simulations. To do so, we fix one

of the three parameters and we simulate the Stokes system (17) and (18) above with different values for the remaining ones. The set of absolute values used for the parameters is  $\{0, 10^2, 10^4\}$  with signs taken as previously described. According to Fig. 10, the effect of high  $\beta$  values is similar to a no-slip boundary condition on  $\Gamma_{sl}$ . For the  $g$  term, it is clear that a high  $|g|$  ( $g < 0$ ) is equivalent to accelerating the spreading; in order to get fewer constraints, the tangential velocity has to be of the order of  $-g/\beta$ . The  $h$  term creates an upwind force that should be responsible for recoiling, see Figs. 11 and 12, for  $\beta = 0, 10^4$  and different values of  $g$  and  $h$ . Also, because of continuity, Figs. 10 and 13 suggest the presence of a tangential velocity component on the free surface even if coefficient  $h = 0$ , which means that caterpillar-like motion is driven by solid-liquid surface properties as well as by those of the liquid-gas interface. In addition, according to Figs. 12 and 13,  $-g/\beta$  acts differently on the free interface whether the contact angle is greater or less than  $\pi/2$ .

### 5.3 Spreading Phase Using the Shikhmurzaev Model

We consider the spreading phase using Shikhmurzaev’s model and the algorithm presented previously. As mentioned above,  $g$  acts like a control on the position of the triple point. A decrease for  $g < 0$  translates in a faster spreading. If  $g$  is small, this influence is likely not to be seen

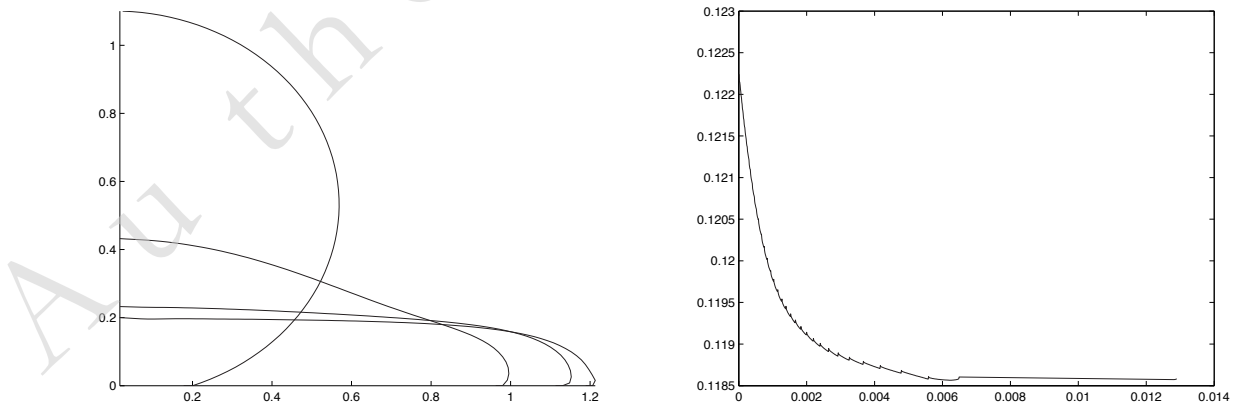
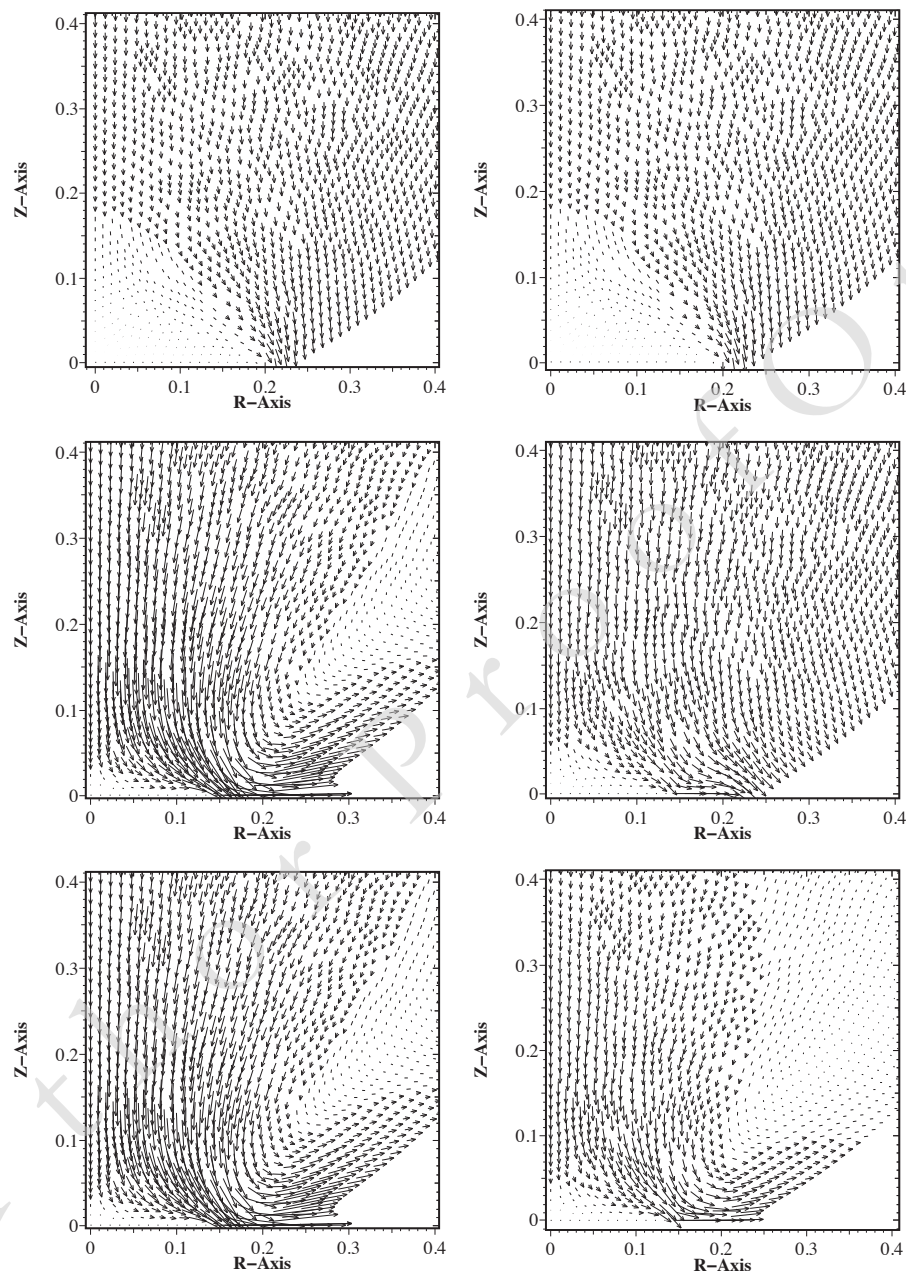
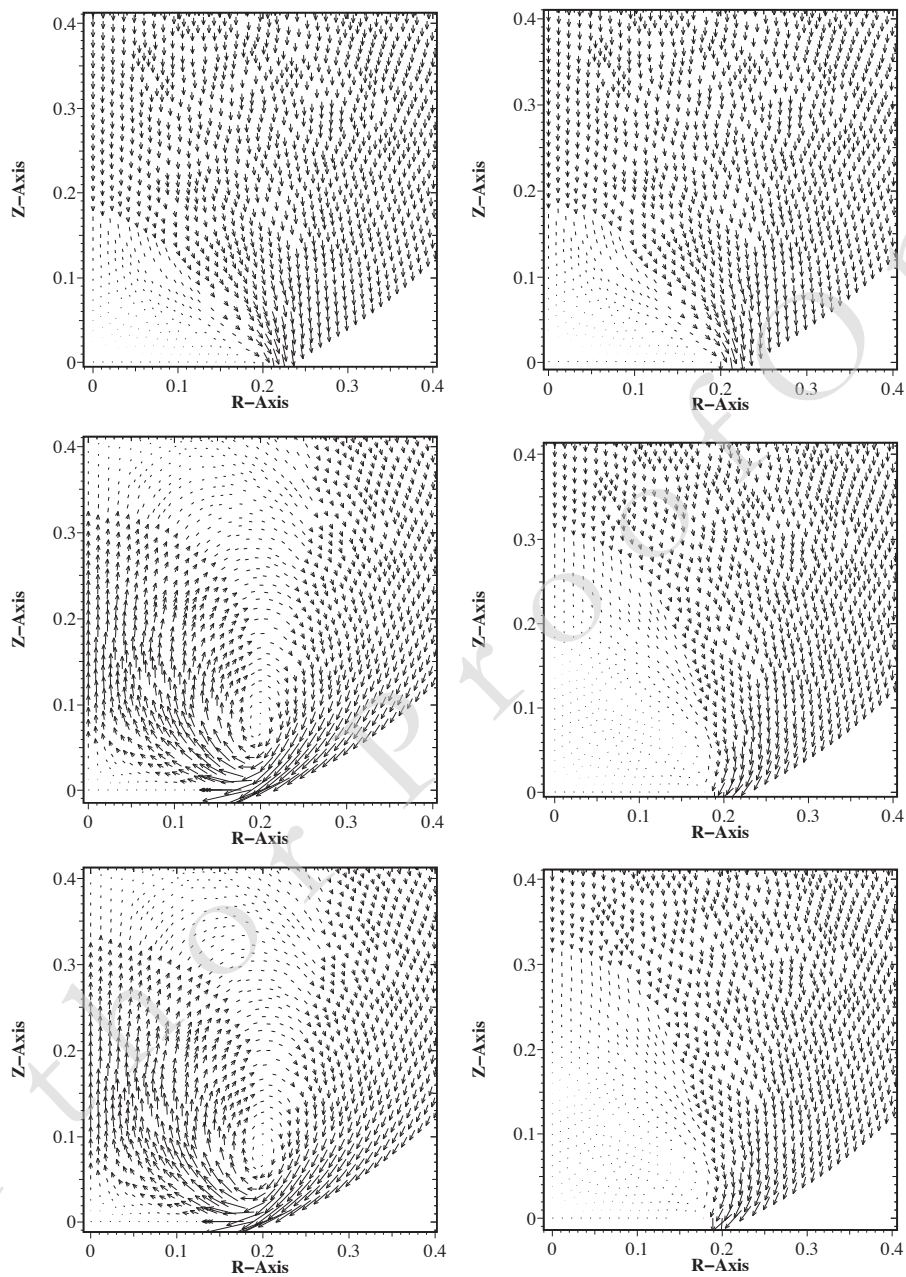


Figure 9. Spreading: droplet profiles and volume in function of time steps



**Figure 10.** Case 1: influence of  $\beta$  and  $g$ ,  $h = 0$ . Velocity in the vicinity of the triple point for  $(\beta, g) = \{(0, 0), (10^4, 0)\}$  (up),  $\{(0, -10^2), (10^4, -10^2)\}$  (middle),  $\{(0, -10^4), (10^4, -10^4)\}$  (down). Scale factors are 3, 3, 0.05, 3, 0.0005, 0.05, respectively



**Figure 11.** Case 2: influence of  $\beta$  and  $h, g = 0$ . Velocity in the vicinity of the triple point for  $(\beta, h) = \{(0, 0), (10^4, 0)\}$  (up),  $\{(0, -10^2), (10^4, -10^2)\}$  (middle),  $\{(0, -10^4), (10^4, -10^4)\}$  (down). Scale factors are 3, 0.1, 0.001, respectively

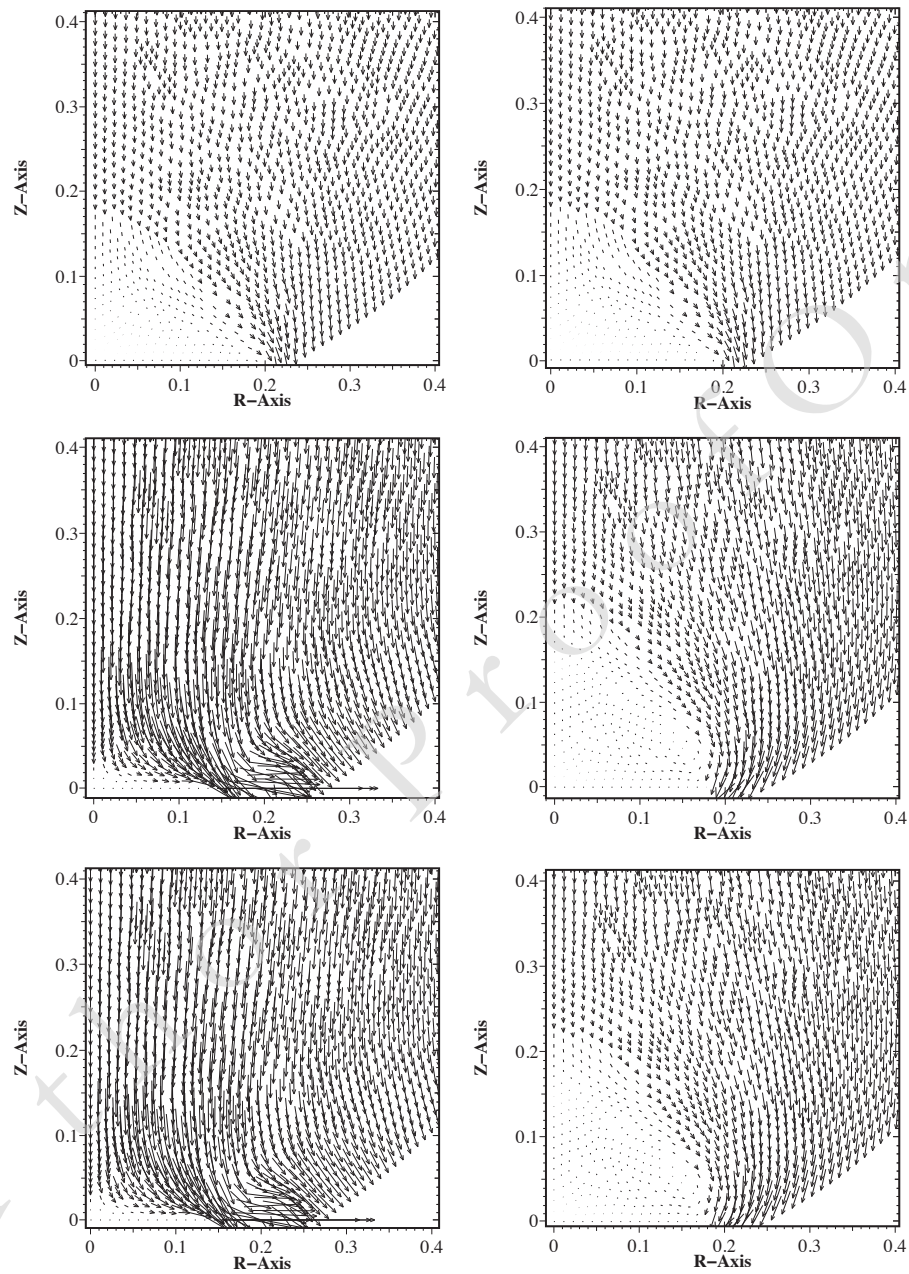


**Figure 12.** Case 3: influence of  $\beta$ ,  $g$  and  $h$ ,  $h = 2g$ . Velocity in the vicinity of the triple point for  $(\beta, g) = \{(0, 0), (10^4, 0)\}$  (up),  $\{(0, -10^2), (10^4, -10^2)\}$  (middle),  $\{(0, -10^4), (10^4, -10^4)\}$  (down). Scale factors are 3, 0.1, 0.001, respectively

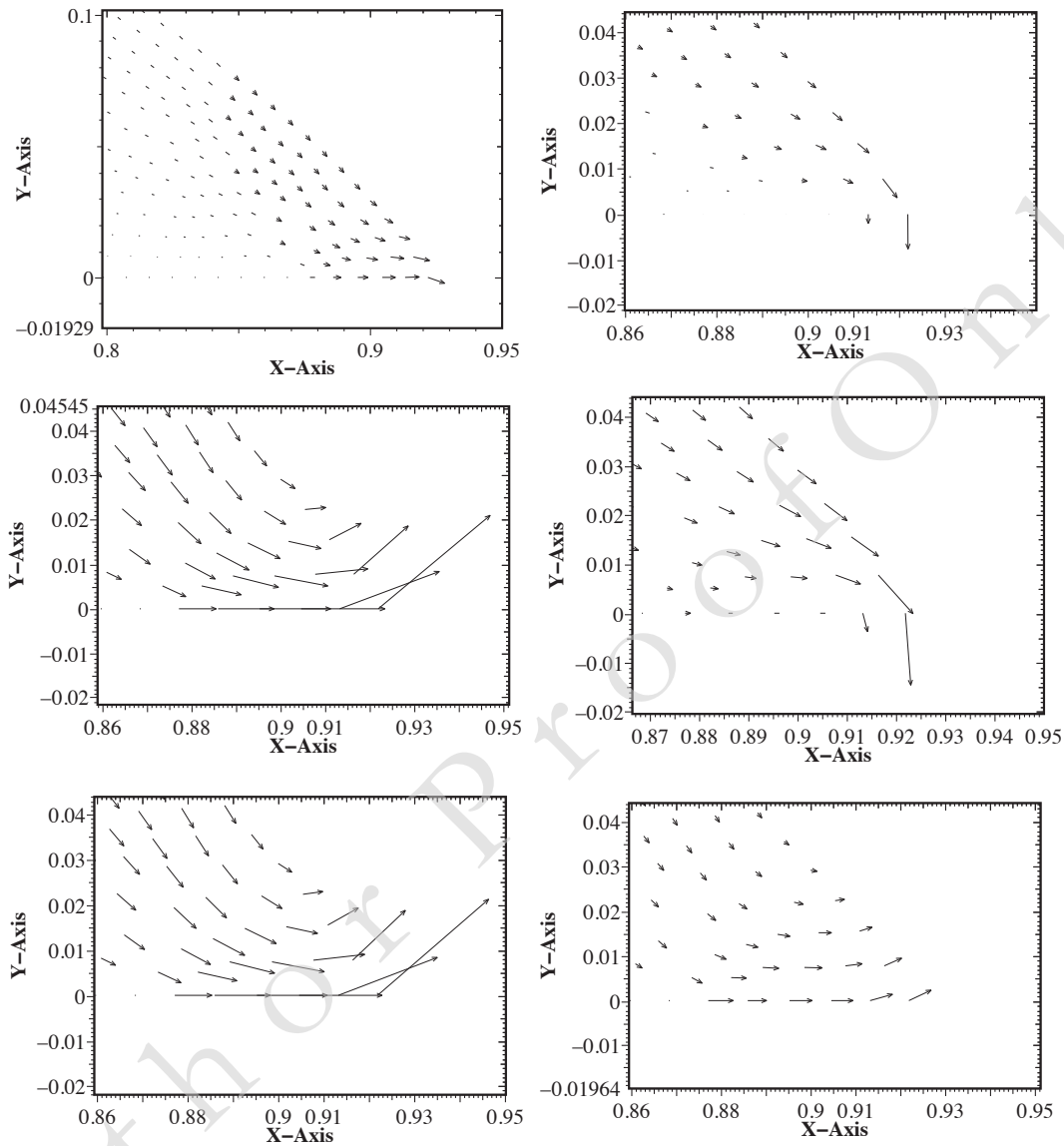


**Figure 13.** Case 3: influence of  $\beta$ ,  $g$  and  $h$ ,  $h = 2g$ . Velocity in the vicinity of the triple point for:  $(\beta, g) = \{(0, 0), (10^4, 0)\}$  (up),  $\{(0, -10^2), (10^4, -10^2)\}$  (middle),  $\{(0, -10^4), (10^4, -10^4)\}$  (down). Scale factors are 0.05, 0.05, 0.005, 0.1,  $5 \times 10^{-5}$ , 0.005, respectively,  $\theta > \frac{\pi}{2}$

in the first part of the spreading, when the inertial forces dominate all other forces in presence. By increasing  $|g|$  over a threshold, which depends on  $\beta$ , it accelerates the spreading and modifies the flow nature. For  $|g|$  large, large interface distortions occur and the mesh generator fails to remesh. In order to observe the influence of the  $g$  term, we fix

$\beta = 1000$ , and we perform 1000 iterations with a step size of  $dt = 5.0 \times 10^{-6}$  for  $g \in \{-10, -100\}$ , Fig. 14. One can observe that after the inertial phase, the triple point position is farther to the right with an increasing  $|g|$  as shown more clearly by Fig. 15.

Figure 16 shows a droplet subjected to large distortion (similar to breakup) when  $|g|$  is getting

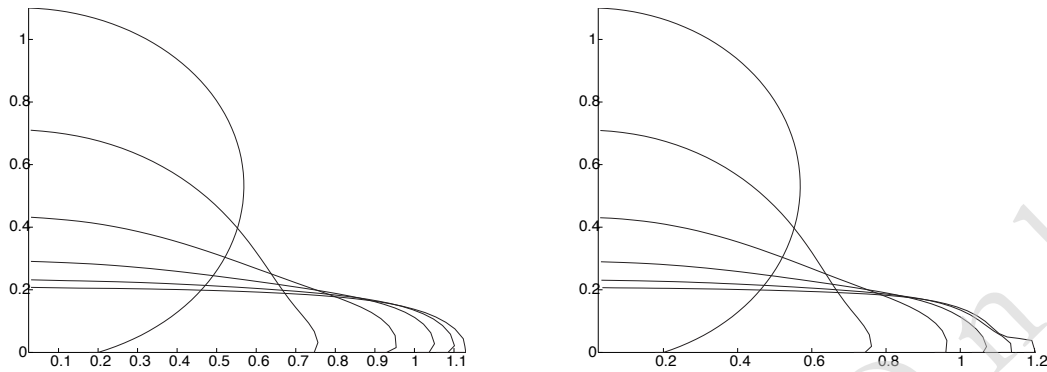


**Figure 14.** Droplet profiles and triple point position (right) for  $(\beta, g) = \{(10^3, -10), (10^3, -10^2)\}$

larger. Simulation can go no further because of the change of topology it implies is not supported by the ALE method we are using.

We try now to see the influence of the sign of parameter  $g$  on the droplet behavior. Since we have seen that parameter  $g$  monitors the spreading, it is also supposed to do so with recoiling. In Fig. 17, simulation is started with an initially spread droplet. Also here, the ratio  $-g/\beta$  significantly influences the behavior of the droplet, while parameter  $h$  influences more particularly the droplet curvature than the triple point position.

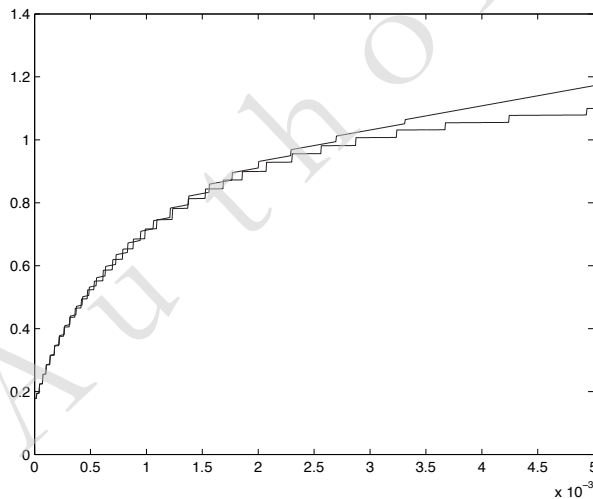


**Figure 15.** Triple point position for  $(\beta, g) = \{(10^3, -10), (10^3, -10^2)\}$

## 6. CONCLUSION

We have discretized and implemented a macroscopic part of the Shikhmurzaev model [7,8], using an ALE formulation and a finite element scheme. Also, a connection with Qian-Wang-Sheng's results [6] has been presented. The present model comprises generalized Navier slip boundary conditions with local surface tension gradient terms in the vicinity of the contact line. The local term values have been chosen based on a previous mathematical and numerical study done in [10]. To test the efficiency of the present algorithm, we first considered a classical mobility relation and we obtained spreading droplet profiles qualitatively comparable to experimental results. Then, we showed how the introduction of these new local terms in the vicinity of the contact line allow modeling the spreading phase. Concerning the recoiling phase, further investigation to implement algorithm our properly is in progress. Also, a full coupling between the macroscopic part and the microscopic part of the Shikhmurzaev model is under progress.

## ACKNOWLEDGMENTS

This study has been co-funded by a research program led by Prof. A. Soucemarianadin (UJF Grenoble). The authors would like to thank J.-L. Achard (CNRS, LEGI Grenoble) for his encouragement. Also, the authors would like to express their gratitude to J. Billingham from the University of Nottingham, England, for his fruitful remarks related to the mesoscopic local surface model.

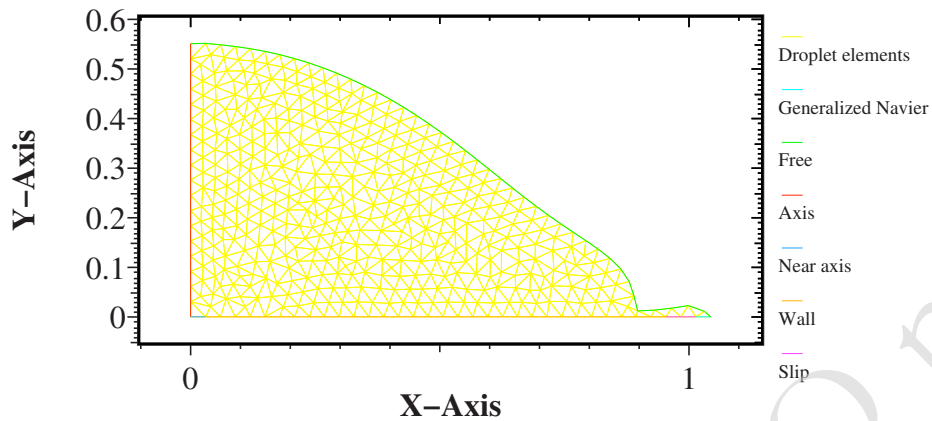


Figure 16. Large interface distortion, similar to a droplet breakup  $g = 10^4$

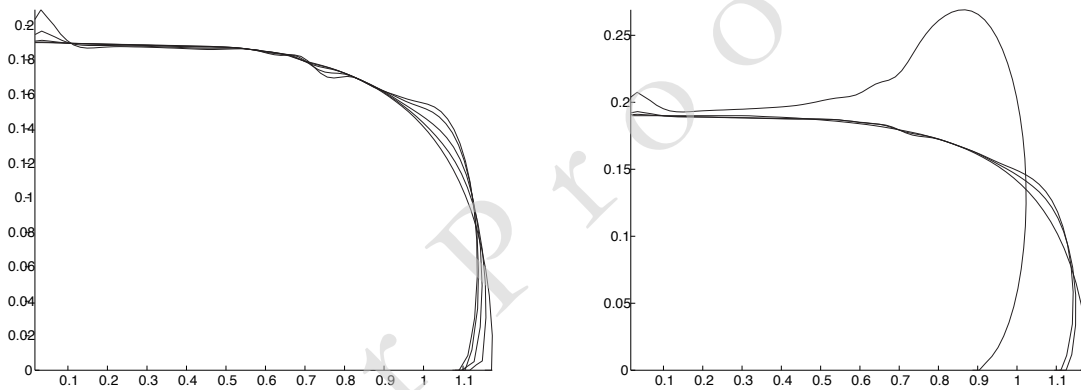


Figure 17. Droplet profiles and triple point position (right) for  $(\beta, g, h) = \{(500, 100, 0), (100, 100, -10)\}$

## REFERENCES

- 1 Dussan, V. E. B., and Davis, S. H., On the motion of a fluid-fluid interface along a solid surface, *J. Fluid Mech.* **65**:71–95, 1974.
- 2 Hocking, L. M., A moving fluid interface. Part II. The removal of the force singularity by a slip flow., *J. Fluid Mech.* **79**:209–229, 1977.
- 3 De Gennes, P. G., Wettings: Statics and dynamics, *Rev. Modern Phys.* **57**:827–863, 1985.
- 4 Jacqmin, D., Contact-line dynamics of a diffuse fluid interface, *J. Fluid. Mech.* **402**:57–88, 2000.
- 5 Pomeau, Y., Recent progress in the moving contact line problem: A review. *C. R. Mécanique.* **330**:207–222, 2002.
- 6 Qian, T., Wang, X.-P., and Sheng, P., Generalized Navier boundary condition for the moving contact line, *Commun. Math. Sci.* **1**:333–341, 2003.
- 7 Blake, T. D., Bracke, M., and Shikhmurzaev, Y. D., Experimental evidence of nonlocal hydrodynamic influence on the dynamic contact angle, *Phys. Fluids.* **11**:1995–2007, 1999.
- 8 Shikhmurzaev, Y. D., The moving contact line problem on a smooth solid surface, *Int. J. Multiphase Flow.* **19**: 589–610, 1993.
- 9 Monnier, J., Modélisation Numérique de la Ligne Triple, Internal Report LMC-IMAG, Summer school CEA Grenoble. Sept., 2003.

- 10 Monnier, J., and Witomski, P., Analysis of a local hydrodynamic model with marangoni effect, *J. Sci. Comp.* **21**:369–403, 2004.
- 11 Hughes, T. J. R., Liu, W., and Zimmermann, T. K., Lagrangian-Eulerian finite element formulation for incompressible viscous flows, *Comp. Methods Applied Mech. Eng.* **29**:329–349, 1981.
- 12 Maury, B., and Pironneau, O., Characteristics ALE method for unsteady free surface flows with surface tension, *Z. Angew. Math. Mech.* **76**:613–696.
- 13 Qian, T., Wang, X.-P., and Sheng, P., Molecular hydrodynamics of the moving contact line in two-phase immiscible flows, *Commun. Comput. Phys.* **1**:1–52, 2006.
- 14 Billingham, J., A reappraisal of a model for the motion of a contact line on a smooth solid surface, *Eur. J. Appl. Math.* **2**:1–10, 2006.
- 15 Saramito, P., Roquet, N., and Etienne, J., Rheolef: The finite element system, <http://www-lmc.imag.fr/lmc-edp/Pierre.Saramito/rheolef/>
- 16 Meyer, M., Desbrun, M., Schröder, P., and Barr, A. H., Discrete differential-geometry operators for triangulated 2-manifolds. In *Visualization and Mathematics III*, Hege, H.-C., and Polthier, K. Eds., 57–xxx, 2003.
- 17 Hamann, B., Curvature approximation for triangulated surfaces. In *Geometric modelling*, Farin, G., et al., Ed. Springer-Verlag, Berlin, 139–153, 1993.
- 18 Allaman, S., Desie, G., Vadiello, D., and Souce-marianadin, A., Impact and spreading of micro-drops onto solid substrates, *Mecaniques Ind.* **4**:443–455, 2003.